nature geoscience
SUPPLEMENTARY INFORMATION
DOI: 10.1038/NGEO2993
In the format provided by the authors and unedited.

Remote detection of widespread indigenous water in lunar pyroclastic deposits

Ralph E. Milliken[1] & Shuai Li[1*]

Affiliations:
[1]Department of Earth, Environmental, and Planetary Sciences, Brown University, Providence, RI 02912

*Correspondence to: njushuaili@gmail.com

Contents of this file:
Supplementary Text
Supplementary Figures 1-6
Supplementary Tables 1-5

Mapping of water in lunar pyroclastic deposits

Assumptions of Grain Size for the Lunar Surface

Based on our laboratory and numerical simulations it is clear that the ESPAT-wt.%H_2O trend is dependent on particle size (see Methods). However, only several locations on the Moon have been directly sampled, and none of these locations correspond to the large, regional dark mantle deposits (DMDs) discussed here. Actual mean grain sizes and ranges, including those for glass beads at regional DMDs, thus remain unknown for much of the lunar surface. Grain size and sorting in returned Apollo samples have been measured and are summarized in (21), where it is noted that the mean grain size of lunar soils ranges from 40-800 μm and most mean values fall between 45-100 μm. Based on the latter, we have adopted an average particle size of 60-80 μm to represent the lunar surface (regolith) in our study, a range that falls within the typical measured values for lunar soils. It has also been observed that glass-rich samples (e.g., green glass from Apollo 15 and orange glass/black beads from Apollo 17) exhibit smaller mean grain sizes than typical lunar soils, closer to a mean value of ~40 μm[21]. To be conservative we have adopted the same ~60-80 μm grain size for the dark mantle deposits, though adopting smaller values (e.g., 40 μm) would result in higher estimates of H_2O content.

Though Apollo pyroclastic-rich materials are better sorted and exhibit smaller mean grain sizes than typical lunar soils[21], it has also been shown that the finer (<25 μm) size fraction of soils is the one most similar to spectra of bulk soils at visible and near-infrared wavelengths[50] (though all components will contribute to the observed spectral signature to some degree). Therefore, although typical lunar soils have larger mean grain sizes than pyroclastic-rich soils, it is possible that the spectral behavior of these two soil types is similar in terms of their 'effective' grain size. However, these grain size effects were evaluated only for lab spectra for wavelengths <2.6 μm, not for the OH/H_2O-bearing 3 μm wavelength region, and it is possible that the spectrally dominant size fraction varies with wavelength. In addition, water may be preferentially hosted in agglutinates[22], which tend to be larger particles and more volumetrically abundant in coarser size fractions of lunar soils[50]. If correct, this would suggest that the water absorptions observed in the 3 μm region of M^3 data are more representative of the large size fraction of lunar soils and not the 'finest fraction'.

These issues highlight the complexity of linking particle size for lunar regolith materials to spectral observations. For the purpose of this study, a key question is whether or not the proposed differences in water content between pyroclastic deposits and surrounding terrains ('typical' lunar regolith) can be explained simply by differences in particle size. The most extreme case would be to assume fine particles dominate the 3 μm spectral region for typical highland/mare regolith whereas large particles dominate the same wavelength region for DMDs. As an example, ~90% of M^3 pixels within the ±35° latitude zone exhibit EPAT values between 0 - 0.01, which would yield an estimate of 0 ~ 60 ppm H_2O assuming 60-80 μm diameter particles. If it is instead assumed that a finer fraction is the spectrally dominant carrier of the water signature for these regions, then an assumed particle size of <45 μm would yield an upper limit of ≤180 ppm H_2O for soils in this latitude zone. In contrast, ESPAT values for pyroclastic deposits approach values of 0.04-0.06. For these regions to exhibit a similar water content of 180 ppm the spectrally dominant particle size at ~3 μm would need to be on the order of ≥100 μm, or ≥2.5 times the mean particle size that has been measured for actual glass-rich Apollo soils. This is an unlikely scenario given that both DMDs and surrounding regions are subject to micrometeorite bombardment and comminution and that measurements of returned samples indicate glass-rich soils exhibit smaller mean grain sizes than typical lunar soils, as described above.

We also note that the majority of M^3 spectra within the ±30° latitude zone exhibit no or very weak absorptions near 3 μm (e.g., ESPAT values close to 0; see Fig. 3b), thus they would always yield H_2O contents at or close to 0 ppm regardless of which values are assumed for particle size. In contrast, spectra for pyroclastic deposits exhibit clear water absorptions and are thus more hydrated than surrounding terrains. This is particularly clear at large DMDs such as Aristarchus, Harbinger, Rima Bode (see Fig. 1) and at smaller DMDs such as those shown in Fig. 2, where ESPAT values are 0 (no absorption band observed) in terrains that surround the pyroclastic deposits. Together, these observations indicate that pyroclastic deposits are preferentially enriched in OH/H_2O compared with typical lunar regolith in the ±35° latitude zone. Though currently lacking, grain size measurements of directly sampled DMD materials would provide the best constraint on estimates of absolute water content for these deposits. Variations in estimated water content as a function of assumed particle size can be evaluated by using the slopes and trends presented in Supplementary Figure 2. If ~100-125 μm diameter particles are preferred, for example, then the ESPAT values for figures shown here should be multiplied by 0.34.

Application to M^3 Data and Comparison with Previously Mapped DMDs

As noted in the main text, the majority of pyroclastic deposits (Dark Mantle Deposits, DMDs) classified as 'very large' and 'large' by Gaddis et al.[18] exhibit evidence of increased water content compared to surrounding terrains, as do many smaller deposits, including several that were recently identified by Gustafson et al.[19]. In the case of the latter, our results confirm that some of these deposits are likely to be related to volatile-driven pyroclastic eruptions. The relationship between our water content maps and previously reported 'very large' pyroclastic deposits is presented in Supplementary Fig. 3, where the numbers correspond to the deposits listed in Supplementary Table 5 (locations and areas are from Gaddis et al.[18]). A close-up view of water associated with dark mantle deposits at Orientale is presented in Supplementary Fig. 4, and histograms of estimated water contents for select deposits are presented in Supplementary Fig. 5. The histograms demonstrate that a significant number of M^3 pixels for each deposit are above an assumed background level of 100 ppm (estimated background water due to solar wind has not been removed in these plots). Absolute water content estimates are based on an assumption of 60-80 μm average diameter regolith particles; histograms would shift to lower values assuming larger particles and higher values assuming smaller particles. Based on this particle size, it is clear that most pixels with these pyroclastic deposits contain <400 ppm OH/H_2O (after subtracting 100 ppm of background). Not all previously mapped pyroclastic deposits are visible at the global/regional scale of Supplementary Figs. 3-4 (see examples of smaller deposits in Fig. 2). Sinus Aestuum, for example, does exhibit a small region of enhanced water content, as shown in Supplementary Fig. 6, but this region is much smaller than previously reported extents of this deposit. This indicates that Sinus Aestuum is less hydrated than other pyroclastic deposits of similar areal extent.

Compilation of Water Contents Measured in Lunar Samples

The data presented in Supplementary Fig. 2c for lunar samples is a compilation of previously published values[51-59]. Results from select pyrolysis measurements that were performed on lunar regolith, mineral separates, agglutinates, and rocks sampled from the Apollo 11, 12, 14, 15, 16, and 17 landing sites are presented in Supplementary Table 3. For comparison with pyrolysis measurements, SIMS results for Apollo 11 agglutinate, Apollo 15 volcanic glasses, Apollo 16 agglutinate, and Apollo 17 agglutinate and volcanic glasses are presented in Supplementary Table 4. It has been argued that water observed in these agglutinates are largely the product of solar wind processes[22], whereas water observed in the volcanic glasses are indicative of water in magma source regions[5-6].

For pyrolysis results, only water amounts measured from temperatures above 300°C are included in order to minimize potential effects of adsorbed terrestrial water. However, it must be considered that all data may suffer from some degree of terrestrial contamination that could introduce large uncertainties in the δD values (where $\delta D=[(D/H)_{sample}/(D/H)_{standard} - 1] \times 1000$), which is one of the most important indices used to determine the origin of lunar water[6,22,51-59]. Indeed, the large range in δD values from the pyrolysis approach, some of which overlap terrestrial values, have been considered an indication of likely terrestrial contamination[51-57]. However, recent measurements on soil grains and agglutinate also confirm that these materials contain water originating from solar wind implantation[22-23]. Regardless of origin, it can be seen that the average water content of examined Apollo samples is 63.0 ppm (Supplementary Tables 1-2 and Supplementary Fig. 2), with most values <100 ppm. Therefore, we adopt a value of 100 ppm to represent lunar surface water that is likely attributable to solar wind processes. Values above this threshold at equatorial latitudes are considered to exhibit 'excess' water from other sources.

References

50. Pieters, C., Fischer, E., Rode, O. & Basu, A. Optical effects of space weathering: the role of the finest fraction. *Journal of Geophysical Research* **98**, 20817-20824 (1993).

51. Epstein, S. & Taylor Jr., H. The concentration and isotopic composition of hydrogen, carbon and silicon in Apollo 11 lunar rocks and minerals. *Proceedings of the Apollo 11 Lunar Science Conference, Supplement in Geochemica et Cosmochimica Acta* **1**, 1085-1096 (1970).

52. Epstein, S. & Taylor Jr., H. O18/O16, Si30/Si28, C13/C12 and D/H studies of Apollo 14 and 15 samples. *Proceedings of the Third Lunar Science Conference, Supplement 3 in Geochirnica et Cosmochimica Acta* **2**, 1429-1454 (1972).

53. Epstein, S. & Taylor Jr., H. The isotopic composition and concentration of water, hydrogen, and carbon in some Apollo 15 and 16 soils and in the Apollo 17 orange soil. *Proceedings of the Fourth Lunar Science Conference, Supplement 4 in Geochimica et Cosmochimica Acta* **2**, 1559-1575 (1973).

54. Friedman, I., O'neil, J. R., Adami, L. H., Gleason, J. D. & Hardcastle, K. Water, hydrogen, deuterium, carbon, carbon-13, and oxygen-18 content of selected lunar material. *Science* **167**, 538-540 (1970).

55. Friedman, I., O'Neil, J. R., Gleason, J. D. & Hardcastle, K. The carbon and hydrogen content and isotopic composition of some Apollo 12 materials. *Proceedings of the Second Lunar Science Conference, MIT Press* **2**, 1407-1415 (1971).

56. Friedman, I., Hardcastle, K. G. & Gleason, J. D. Water and carbon in rusty lunar rock 66095. *Science* **185**, 346-349 (1974).

57. Merlivat, L., Lelu, M., Nief, G. & Roth, E. Deuterium, hydrogen, and water content of lunar material. *Proceedings of the Fifth Lunar Science Conference, Supplement 5 in Geochimica et Cosmochimica Acta* **2**, 1885-1895 (1974).

58. Greenwood, J. P. et al. Hydrogen isotope ratios in lunar rocks indicate delivery of cometary water to the Moon. *Nature Geoscience* **4**, 79-82 (2011).

59. Saal, A., Hauri, E., Van Orman, J. A. & Rutherford, M. Hydrogen isotopes in lunar volcanic glasses and melt inclusions reveal a carbonaceous chondrite heritage. *Science* **340**, 1317-1320 (2013).

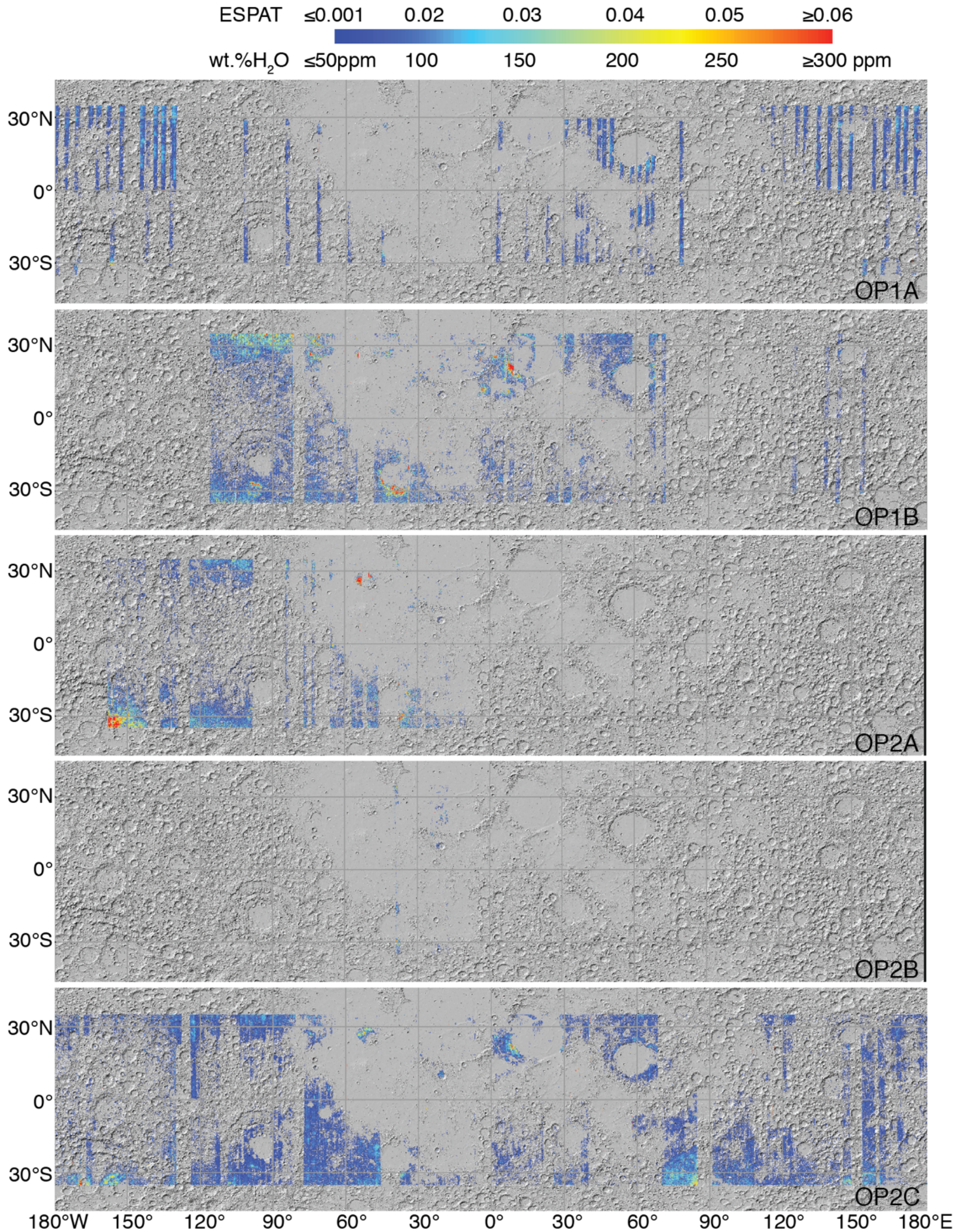

Supplementary Fig. 1. ESPAT/water content maps derived from M3 data broken down by optical period. Water content values are based on the assumption of 60-80 µm diameter particles; estimated solar wind background value of 100 ppm has not been subtracted.

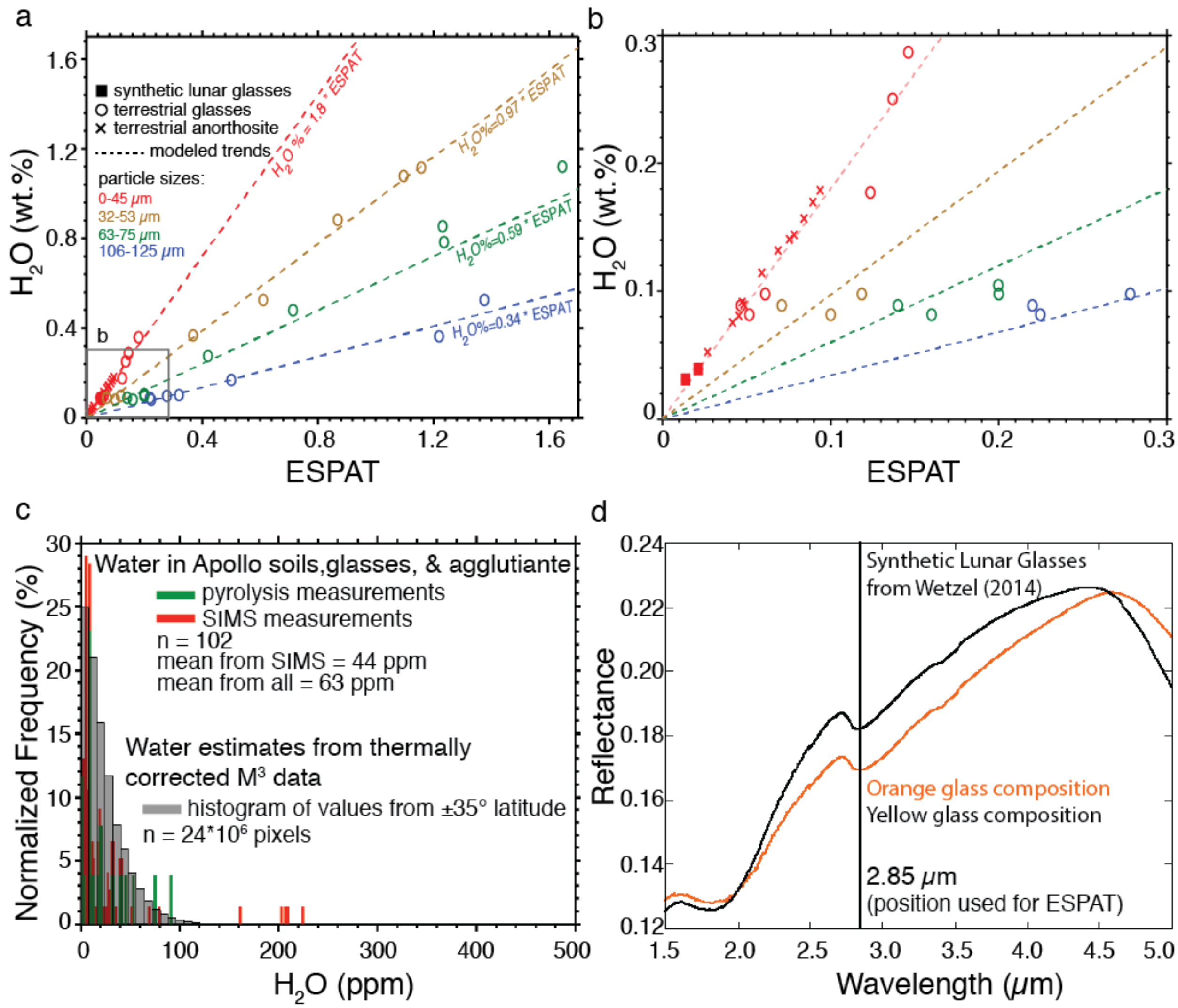

Supplementary Fig. 2. Data used to estimate ESPAT-wt.%H_2O trend for volcanic glasses and estimates of lunar background water content. (a) Terrestrial anorthosite, terrrestrial MORB glasses, and synthetic glasses of lunar composition define linear ESPAT-H_2O trends for which the slope varies with particle size (symbols). Similar trends are predicted from forward-modeled reflectance spectra using measured extinction coefficients for volcanic glass (dashed lines). (b) zoomed-in portion outlined by gray box in (a) showing similarity between measured and calculated values at low water content; water contents are similar for different colors because the same samples were used to evaluate particle size effects. (c) Histogram of water contents from M^3 data (gray bars) in the ±30° latitude zone assuming 60-80 µm diameter particles from trend shown in (a). Water in lunar samples determined by pyrolysis and SIMS measurements are shown for comparison. Typical values for M^3 in this zone are <100 ppm, similar to water losses observed in pyrolysis measurements and likely attributable to a solar wind origin. (d) Example laboratory reflectance spectra for synthetic orange and lunar glasses showing broad OH/H_2O absorption near ~3 µm. Wavelength position for ESPAT calculation (2.85 µm) is marked and is near the maximum absorption point. RELAB sample IDs RM-REM-139A and RM-REM-140A.

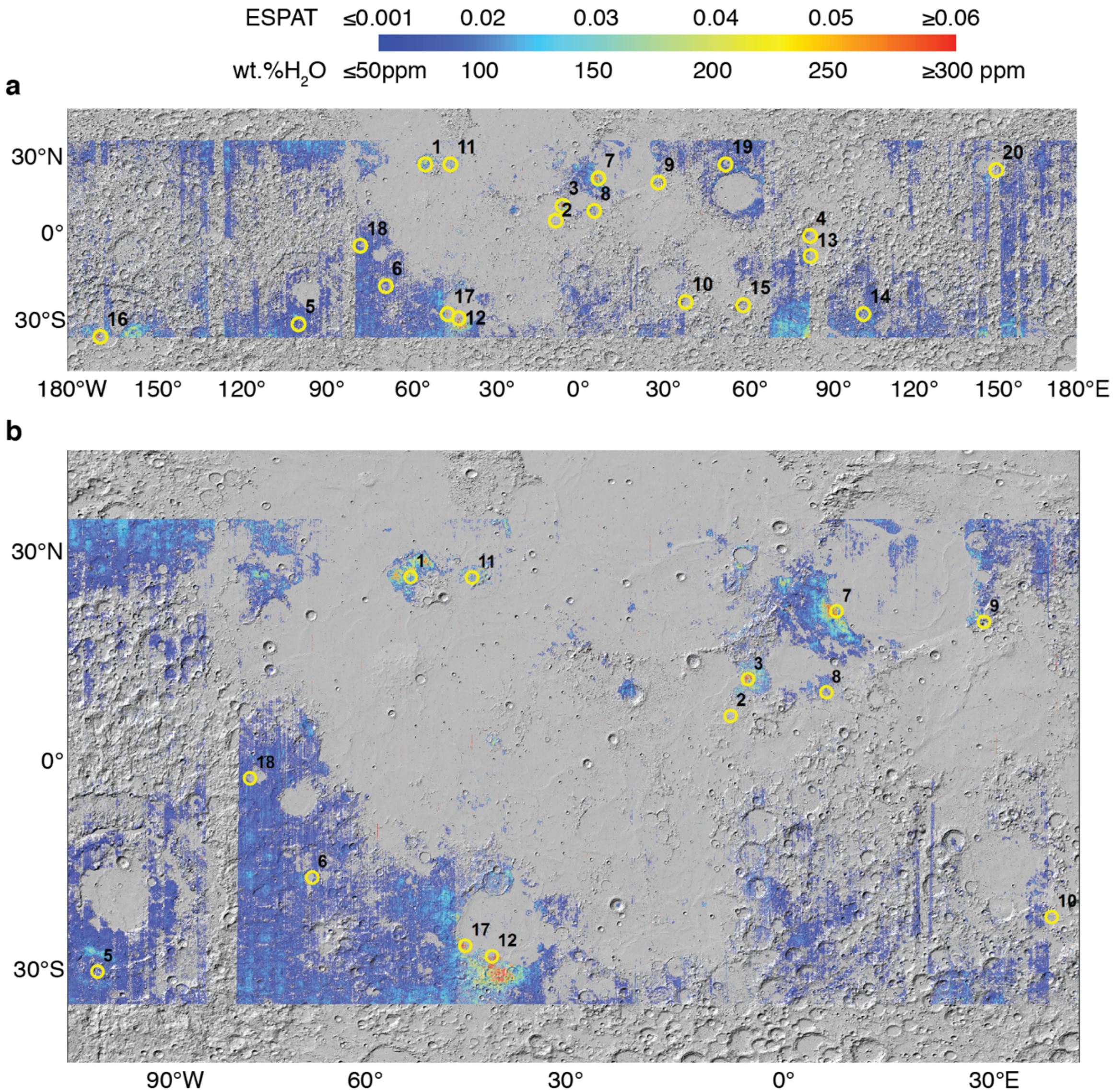

Supplementary Fig. 3. ESPAT/water content maps derived from M3 data (all optical periods) compared with distribution of 'very large' pyroclastic deposits listed in Gaddis et al.[18]. Water content values are based on the assumption of 60-80 µm diameter particles; estimated solar wind background value of 100 ppm has not been subtracted. a) global view for latitude zone ±35°. b) zoomed-in view for a portion of the nearside of the Moon. Numbers correspond to pyroclastic deposits listed in Supplementary Table 5. Though not visible at the scale of these maps, nearly all of the numbered deposits exhibit some degree of enhanced hydration relative to surrounding terrains.

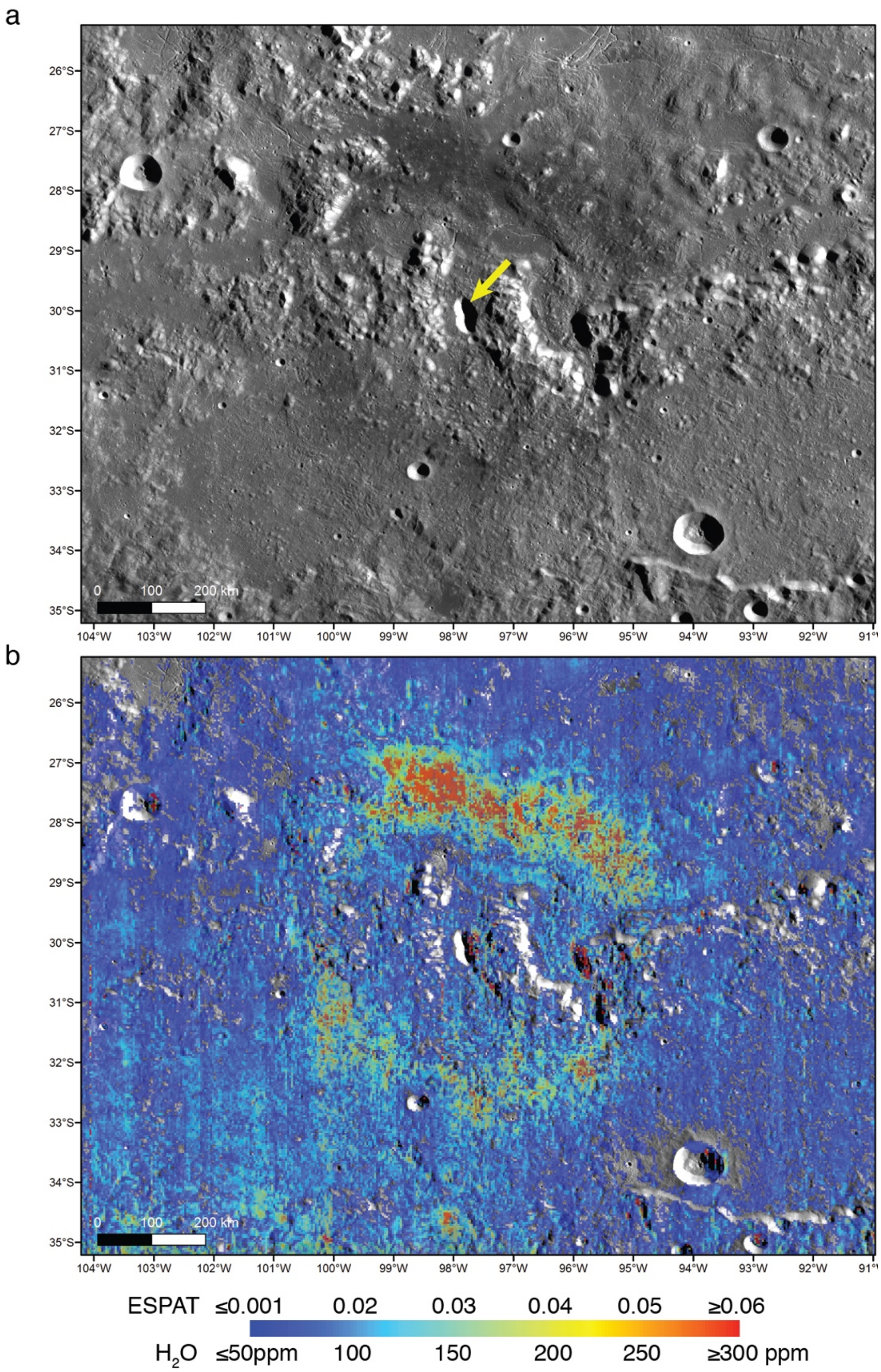

Supplementary Fig. 4. Dark mantle deposits inferred as pyroclastic deposits along southwestern rim of Orientale. a) LROC wide-angle camera (WAC) image showing dark materials ringing a potential vent (yellow arrow); b) ESPAT/H_2O map overlain on image shown in (a).

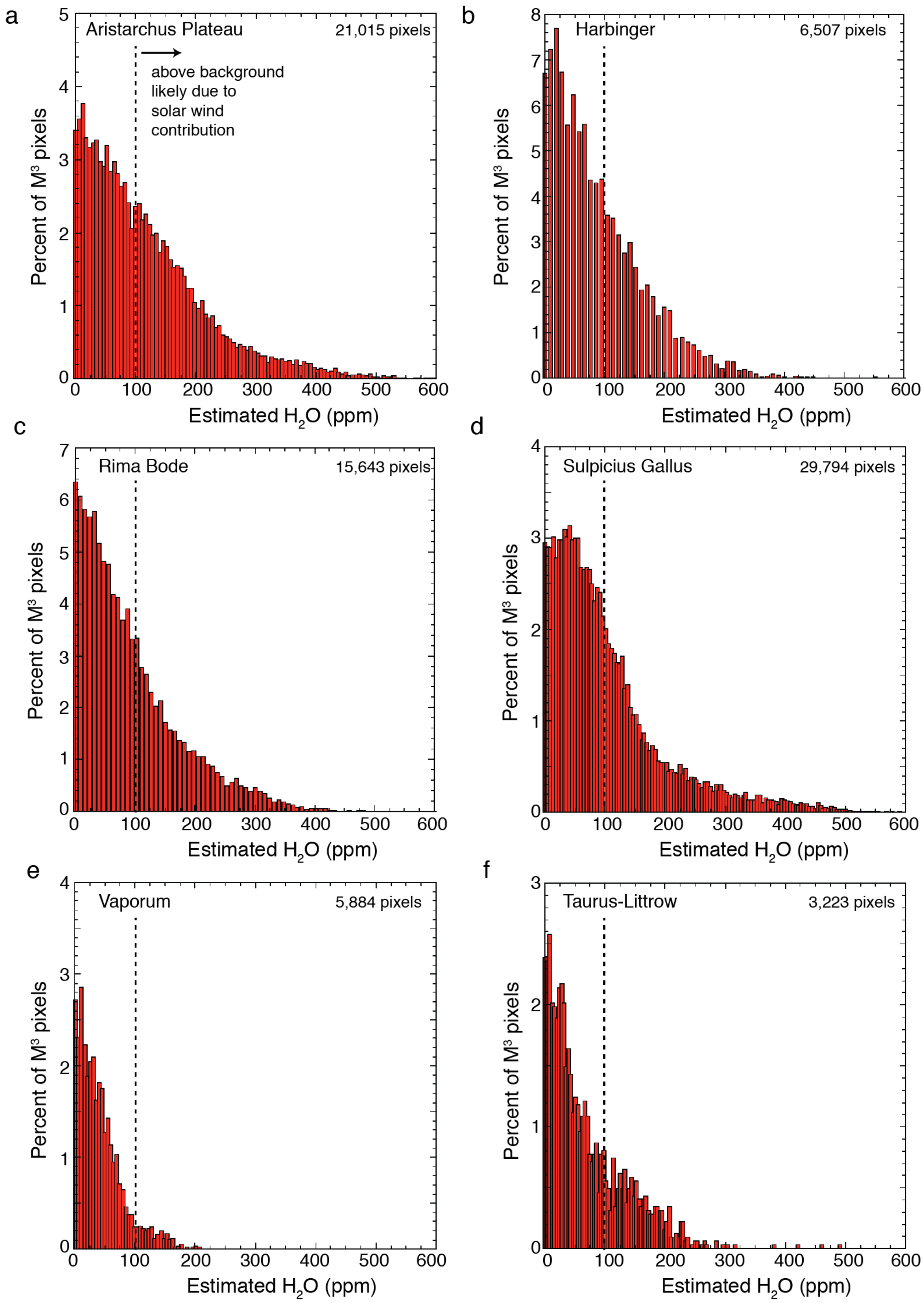

Supplementary Fig. 5. Histograms of estimated water content values for select pyroclastic deposits. Values are based on the assumption of 60-80 µm diameter particles. All pixels may include ~100 ppm of water attributable to solar wind implantation, but numerous pixels are beyond this value for these deposits. Pixels in these regions with values of 0 (no water absorption feature) were not included in this analysis.

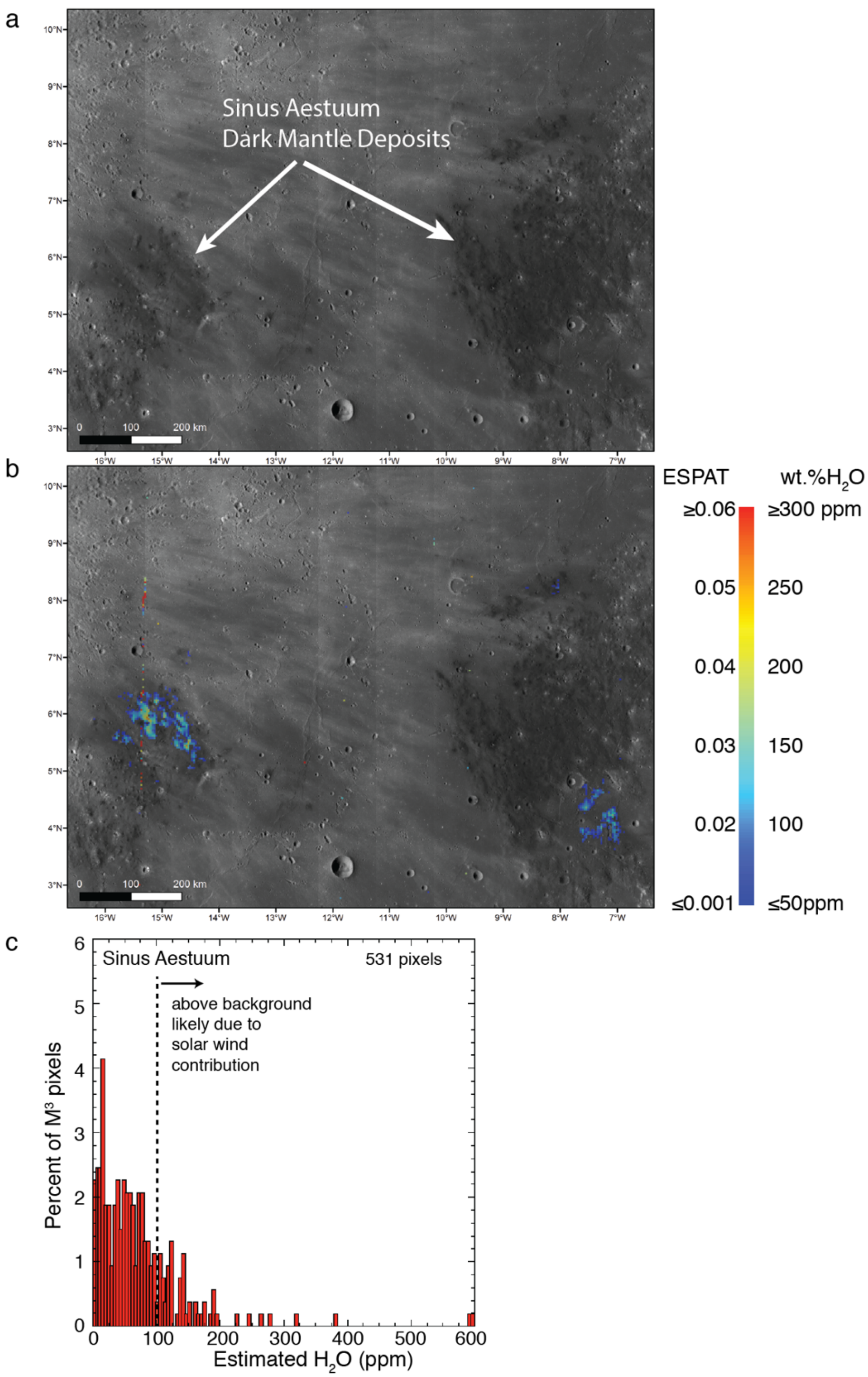

Supplementary Fig. 6. Water content of pyroclastic deposits at Sinus Aestuum. a) Lunar Reconnaissance Orbiter Camera wide angle (WAC) image showing locations of dark mantle deposits inferred to be pyroclastic deposits. b) ESPAT/H_2O map (1 km/pixel) overlain on WAC image. Note that most of the dark mantle material does not exhibit evidence for increased water content. c) Histogram of water contents for map shown in (b); very few pixels are above the estimated ~100 ppm solar wind background at this spatial scale, indicating this deposit contains less water than other large pyroclastic deposits. Pixels with values of 0 (no water absorption feature) were not included in this analysis.

Supplementary Table 1. Water contents for terrestrial mid-ocean ridge basalt glasses corresponding to data shown in Supplementary Fig. 2.

Sample Name	Initial Water Content (ppm)	Reference
D9A	976.49	[*Shimizu et al.*, 2015]
D38A	16227.00	
D44A	815.44	
D44B	888.00	

Supplementary Table 2. Water contents for glasses of synthetic lunar composition used to derive ESPAT-wt.%H_2O trends and corresponding to data shown in Supplementary Fig. 2.

Sample Name	Water Content (ppm)	Reference
Orange glass (OGV-5)	390	[*Wetzel*, 2014]
Yellow glass (YG-5)	305	

Supplementary Table 3. Water contents and δD values for Apollo regolith, rock, and mineral samples measured via pyrolysis corresponding to data shown in Supplementary Fig. 2.

Reference	Sample Name	H_2O (ppm)	δD (‰)	Temperature
Merlivat et al., 1974	15600 regolith	46.8	-59	>600°
	15600 regolith	68.4	-95	
	68501 regolith	93.6	-115	
	72501 regolith	90	-88	
	72501 regolith	82.8	-82	
	78501 regolith	104.4	-72	
	15229 agglutinate	228.6	-52	
	15229 agglutinate	7.2	-242	
	70215 basalt	48.6	-165	
	75035 basalt	44.6	-92	
	75035 basalt	50.4	-252	
Epstein and Taylor, 1973	15021.4 regolith	48.6	-252	630°-melting
	64421.21 regolith	109.8	-280	500°-melting
	65513.1 regolith	268.2	-173	500°-melting
	62221.8 regolith	199.8	-88	500°-melting
	74220.22 regolith	46.8	-154	500°-melting
Friedman et al., 1971	12030.30 regolith	7	-300	430°-1025°
Friedman et al., 1970	10046.21 agglutinate	455	-756	300°-950°
	10046.22 agglutinate	372	-576	300°-950°
	10060.11 agglutinate	152	-865	300°-950°
Epstein and Taylor, 1970	10084.2 rock and minerals	90.4	-380	500°-1400°
	10084.1 rock and minerals	208.4	-268	500°-1400°
	10061 rock and minerals	160.2	-409	500°-1400°
Epstein and Taylor, 1972	14422 regolith	48.6	-419	550°-600°
Friedman et al., 1974	66095.62 rock	9	-194	690°-1350°
	66095.31 rock	13.5	-153	690°-1350°

Supplementary Table 4. Water contents and δD values for Apollo glass and agglutinate samples measured via SIMS corresponding to data shown in Supplementary Fig. 2.

Sample Name	H_2O (ppm)	δD (‰)	Reference
10084 Agglutinate	470	4555	Liu et al., 2012
	27	5413	
	225	-562	
	282	-789	
	246	-843	
	161	-731	
	188	191	
	207	267	
70051 Agglutinate	200	-711	
	209	-844	
	203	-781	
64501 Agglutinate	79	-558	
74220 Glass	5.0	446	Saal et al., 2013
	3.5	194	
	4.6	283	
	5.5	412	
	4.6	453	
	4.9	291	
	4.4	235	
	3.8	416	
	3.2	269	
	8.7	392	
	6.7	299	
	5.7	330	
	3.7	406	
	3.1	396	
	3.5	307	
15426 Low Ti glass	69.3	474	
	51.9	347	
	40.7	349	
	39.2	459	
	34.8	804	
	32.7	2199	
	30.8	2258	
	28.1	843	
	27.9	545	
	27.8	2244	
	25.1	502	
	22.8	469	
	22.0	1210	
	16.8	2160	
	16.3	580	
15427 Very Low Ti glass	33.8	578	
	28.6	1802	
	14.4	4045	
	12.1	1043	
	11.4	830	
	10.8	209	
	9.4	761	
	9.1	1028	
	8.7	616	
	7.4	80	
	6.9	371	
	6.4	-378	
	6.2	487	

	6.1	626	
	6.1	2	
	5.7	-616	
	5.6	-93	
	5.5	-119	
	5.5	-213	
	5.5	-139	
	5.3	318	
	5.3	837	
	5.3	50	
	5.1	523	
	4.9	273	
	4.4	-338	
	4.4	-165	
	4.2	2209	
	4.1	-733	
	3.6	-651	

Supplementary Table 5. Locations and areas for lunar pyroclastic deposits classified as 'very large' in Gaddis et al.[18]. Deposit number corresponds to numbers shown in Supplementary Fig. 3.

Deposit #	Name	Latitude	Longitude	Area (km^2)
1	Aristarchus	26.7	-52.3	49013
2	Aestuum	6.6	-5.9	10357
3	RimaBode	11.9	-3.4	6620
4	SmythiiNW	1.1	84.8	5851
5	Orientale	-30.3	-97.5	5321
6	Cruger	-16.7	-66.5	4828
7	Sulpicius Gallus	21.7	9.4	4322
8	Vaporum	10	7.9	4129
9	TaurusLittrow	20.2	30.7	2940
10	Nectaris SE	-22.4	40.5	2905
11	Harbinger	26.6	-43.4	2877
12	Dopplemayer	-28.1	-40.5	2628
13	Smythii SW	-6	85	2539
14	Titius	-26.7	103.9	2159
15	Petavius	-23.5	61	1645
16	Oppenheimer NW	-34.8	-168.2	1500
17	Humorum SW	-26.6	-44.4	1472
18	Riccioli	-2.4	-75.5	1089
19	Cleomedes	26.6	54.7	1084
20	Moscoviense SE	24.7	151.2	1022